Appl Nanosci (2014) 4:1–14
DOI 10.1007/s13204-012-0172-y

ORIGINAL ARTICLE

Prospects of IMPATT devices based on wide bandgap semiconductors as potential terahertz sources

Aritra Acharyya · J. P. Banerjee

Received: 2 July 2012 / Accepted: 30 October 2012 / Published online: 16 November 2012

Abstract In this paper the potentiality of impact avalanche transit time (IMPATT) devices based on different semiconductor materials such as GaAs, Si, InP, 4H-SiC and Wurtzite-GaN (Wz-GaN) has been explored for operation at terahertz frequencies. Drift–diffusion model is used to design double-drift region (DDR) IMPATTs based on different materials at millimeter-wave (mm-wave) and terahertz (THz) frequencies. The performance limitations of these devices are studied from the avalanche response times at different mm-wave and THz frequencies. Results show that the upper cut-off frequency limits of GaAs and Si DDR IMPATTs are 220 GHz and 0.5 THz, respectively, whereas the same for InP and 4H-SiC DDR IMPATTs is 1.0 THz. Wz-GaN DDR IMPATTs are found to be excellent candidate for generation of RF power at THz frequencies of the order of 5.0 THz with appreciable DC to RF conversion efficiency. Further, it is observed that up to 1.0 THz, 4H-SiC DDR IMPATTs excel Wz-GaN DDR IMPATTs as regards their RF power outputs. Thus, the wide bandgap semiconductors such as Wz-GaN and 4H-SiC are highly suitable materials for DDR IMPATTs at both mm-wave and THz frequency ranges.

Keywords Avalanche response time · DDR IMPATTs · Terahertz · Wide bandgap semiconductors

A. Acharyya (✉) · J. P. Banerjee
Institute of Radio Physics and Electronics, University of Calcutta, 92, APC Road, Kolkata 700009 West Bengal, India
e-mail: ari_besu@yahoo.co.in

Introduction

The terahertz (THz) frequency belongs to the region of electromagnetic spectrum in between the wavelengths 1,000 and 30 μm (i.e. 0.3–10 THz). Terahertz sources are in great demand nowadays for various application areas such as spectroscopy (Grischkowsky et al. 1990), biosensing (Debus and Bolivar 2007), quality inspection in various industrial branches (Yasui et al. 2005; Stoik et al. 2008; Jördens and Koch 2008), medical and pharmaceutical applications (Fitzgerald et al. 2005; Siegel 2004), THz astronomy (Siegel 2007), etc. The inherent advantages and potential benefits of the THz frequency regime (0.3–10 THz) for both civilian and defense applications have generated lot of research interest in the development of THz components, sources and detectors. Though the THz region has several applications, lack of suitable THz sources has hindered the developments of THz systems. Most of the available THz sources are complex, bulky and not operational at room temperature except some recently developed THz sources based on cascaded frequency multipliers which are frequency tunable, operational at room temperature and have excellent signal quality. Recently reported 1.9–2.7 THz sources based on cascaded frequency multipliers are capable of generating 10–2 μW of power and these are useful as local oscillators for astronomical receivers (Ward et al. 2004; Heyminck et al. 2009; Crowe et al. 2011a, b; Maestrini et al. 2012). Thus, the power delivering capabilities of these sources are not sufficient to use those as frequency generators in powerful THz transmitting systems.

Among two-terminal solid-state sources impact avalanche transit time (IMPATT) devices have already emerged as high-power, high-efficiency solid-state sources for both microwave (3–30 GHz) and millimeter-wave

(30–300 GHz) frequency bands (Midford and Bernick 1979; Chang et al. 1977; Gray et al. 1969). Si and GaAs IMPATTs are already established as powerful and efficient sources at different millimeter-wave window frequencies (Luy et al. 1987; Dalle et al. 1990; Luschas et al. 2002a, b; Shih et al. 1983; Eisele and Haddad 1995). Eisele et al. (1996) first experimentally demonstrated the InP-based IMPATT operation at W-band. But so far as authors' knowledge is concerned, the experimental results on THz performance of InP IMPATTs are not available in the published literatures. But some recent theoretical study reveals the potentiality of InP-based IMPATTs as THz sources (Mukherjee et al. 2007, 2010). In recent years the potentiality of wide bandgap materials (SiC, GaN) for generation of RF power at THz frequencies has been reported (Mukherjee and Mazumder 2007; Mukherjee et al. 2009; Panda et al. 2007, 2001; Banerjee et al. 2010). Yuan et al. (2001) first demonstrated the 4H-SiC based p^+–n–n^-–n^+ structured IMPATT diode oscillator operating at X-band. Later, Vassilevski et al. (2001) experimentally obtained better RF power output from single-drift region (SDR) p^+–n–n^+ 4H-SiC IMPATT diode oscillator. So far as authors' knowledge is concerned, experimental report on GaN-based IMPATT sources is not reported so far in the published literatures. This may be due to lack of mature fabrication technology of SiC and GaN-based IMPATT devices at mm-wave and THz frequencies.

In the present paper, the authors have studied the millimeter-wave and THz performance of GaAs, Si, InP, 4H-SiC and Wz-GaN-based DDR IMPATTs using an avalanche response time-based analysis (Acharyya and Banerjee 2012, 2013; Acharyya et al. 2012) following a double-iterative field maximum simulation method (Roy et al. 1979, 1985) based on Gummel–Blue model (Gummel and Blue 1967) to obtain the upper cut-off frequencies for IMPATT operation. The high-frequency performance of IMPATT devices depends on the material parameters such as carrier ionization rates (α_n, α_p), saturated drift velocities (v_{sn}, v_{sp}), etc. of the base semiconductors. The avalanche response time of the charge carriers (electrons and holes) is related to the avalanche multiplication process and plays an important role in determining the high-frequency performance of the device. Lower avalanche response time facilitates higher frequency of operation. Thus, the avalanche response times associated with GaAs, Si, InP, 4H-SiC and Wz-GaN based DDR IMPATTs are calculated at different mm-wave and THz frequencies to determine the upper cut-off frequency limits of those devices. DDR structure is preferred over SDR structure for investigation because the presence of two drift layers (n- and p-layers) in DDR structure leads to higher drift zone voltage at a particular frequency of operation as compared with SDR structure in which only one drift layer is available (n- or p-drift layer); and this ensures higher DC to RF conversion efficiency (η) and higher RF power output (P_{RF}) (Sze and Ng 2010). The simulation obtained results are compared with the experimental results to validate the DC and high-frequency simulation technique adopted by the authors to study the mm-wave and THz performance of the DDR IMPATTs based on different semiconductors.

Material parameters and design method

Material parameters

The electric field variation of carrier ionization rates in GaAs, Si, InP and Wz-GaN is given by

$$\alpha_{n,p}(\xi) = A_{n,p} \exp\left[\left(\frac{-B_{n,p}}{\xi}\right)^m\right] \quad (1)$$

where the value of the constant $m = 1$ for Si, InP and Wz-GaN and $m = 2$ for GaAs. The values of the ionization coefficients $A_{n,p}$ and $B_{n,p}$ for a wide field range in GaAs for <100> orientation have been taken from experimental data of Ito et al. (1978). The values of $A_{n,p}$ and $B_{n,p}$ for Si have been taken from the experimental results reported by Grant (1973). The ionization coefficients $A_{n,p}$ and $B_{n,p}$ in <100> InP have been obtained from the experimental data of Kao and Crowell (1980) for the lower field range (2.5×10^7 to 5.0×10^7 V m^{-1}) and Umebu et al. (1980) for the higher field range (5.0×10^7 to 8.0×10^7 V m^{-1}). The same coefficients ($A_{n,p}$ and $B_{n,p}$) of Wz-GaN are taken from recently published report of Kunihiro et al. (1999). The field variation of carrier ionization rates in 4H-SiC is given by

$$\alpha_n(\xi) = \left(\frac{\xi}{A_n}\right) \exp\left(\frac{-B_n}{\xi^2}\right), \quad (2)$$

$$\alpha_p(\xi) = \left(\frac{\xi}{7}\right) \exp\left[\frac{-1}{(A_p\xi^2 + B_p\xi)}\right]. \quad (3)$$

The values of the constants $A_{n,p}$ and $B_{n,p}$ for a wide field range in 4H-SiC are taken from experimentally reported data (Konstantinov et al. 1997). The electron and hole drift velocity versus field characteristics of Si have an experimental field dependence given by

$$v_{n,p}(\xi) = v_{sn,sp}\left[1 - \exp\left(\frac{-\mu_{n,p}\xi}{v_{sn,sp}}\right)\right]. \quad (4)$$

The values of v_{sn} and v_{sp} are taken from the experimental data of Canali et al. (1971). The negative differential mobility in the electron drift velocity versus electric field characteristics of group III-IV semiconductors GaAs (Kramer and Micrea 1975), InP (Kramer and Micrea 1975) and Wz-GaN (Shiyu and Wang 2008) have been

taken into account in the computer simulation through the expression

$$v_n(\xi) = \frac{\left[\mu_n \xi + v_{sn}(\xi/\xi_c)^4\right]}{\left[1 + (\xi/\xi_c)^4\right]} \quad (5)$$

which incorporates a peak in the drift velocity at low field (ξ_c) followed by a velocity saturation at high electric field. The hole drift velocity versus field characteristics of GaAs, InP and Wz-GaN are same as Si as given by Eq. (4). The field dependence of electron and hole drift velocity in 4H-SiC are given by (Vassilevski et al. 2000):

$$v_{n,p}(\xi) = \left[\frac{\mu_{n,p}\xi}{\left(1 + \left(\mu_{n,p}\xi/v_{sn,sp}\right)^{\kappa}\right)}\right]^{1/\kappa}, \quad (6)$$

where the value of $\kappa = 1.20$. All other material parameters such as bandgap (E_g), intrinsic carrier concentration (n_i), effective density of states of conduction and valance bands (N_c, N_v), diffusion coefficients (D_n, D_p), mobilities (μ_n, μ_p) and diffusion lengths (L_n, L_p) of charge carriers and permittivity (ε_s) of the semiconductor materials under consideration are taken from recently published reports (Electronic Archive 2012).

Design method

The frequency of operation of an IMPATT diode essentially depends on the transit time (τ_T) of charge carriers to cross the depletion layer of the device. IMPATT diodes having double-drift region n^+–n–p–p^+ structure are first designed for a particular frequency (f_d) by the transit time formula of Sze and Ryder (1971) given by $W_{n,p} = 0.37\, v_{sn,sp}/f_d$, where $W_{n,p}$ and $v_{sn,sp}$ are the n- or p-side depletion layer widths, saturation velocities of electrons/holes respectively. Here n^+- and p^+-layers are highly doped layers whose doping concentrations are taken to be $N_{n+} = N_{p+} = 10^{26}$ m^{-3}. The background doping concentrations of n- and p-depletion regions (N_D, N_A) are initially chosen according to the design frequency. The electric field profile using the above doping profile is obtained from the DC simulation described in next subsection (Roy et al. 1979). The input doping profile is adjusted so that the electric field just punches through the depletion layers ($W_{n,p}$) for a particular value of f_d and a particular biasing current density (J_0). The high-frequency computer simulation described elsewhere (Roy et al. 1985) based on Gummel–Blue approach (Gummel and Blue 1967) is then carried out to obtain the admittance characteristics of the device. The peak optimum frequency (f_p) corresponding to the peak negative conductance is determined from the admittance characteristics. If the magnitude of f_p differs very much from f_d, the value of J_0 is varied and the computer simulation program is run till the value of f_p is nearly equal to the value of f_d. The bias current density is thus fixed for the particular design frequency. Realistic doping profile for flat profile diode has been used for the present analysis. The doping profile at the interfaces of epitaxy and substrate (n^+n-interface) is approximated as error function. The doping profile near the p^+p-interface has been made realistic by suitable exponential functions. Structural and doping parameters of the designed DDR IMPATTs based on GaAs, Si, InP, 4H-SiC and Wz-GaN are listed in Table 1.

Simulation technique

One-dimensional model of reverse biased n^+–n–p–p^+ lateral DDR IMPATT structure, shown in Fig. 1, is used to simulate the DC and high-frequency properties of the device under optical illumination. The physical phenomena take place in the semiconductor bulk along the symmetry axis of the DDR IMPATT devices. Thus, the one-dimensional model of IMPATT devices considered in this work is justified.

DC simulation

The DC electric field and normalized current density profiles in the depletion layer of the device are obtained from simultaneous numerical solution of fundamental device equations such as Poisson's equation, combined carrier continuity equation, current density equations and mobile space charge equation subject to appropriate boundary conditions (Acharyya and Banerjee 2012). A double-iterative field maximum simulation method based on Gummel–Blue approach (Gummel and Blue 1967) described elsewhere (Roy et al. 1979; Acharyya and Banerjee 2012) is used to solve these equations and obtain the electric field and normalized current density profiles. In the above-mentioned simulation method, the computation starts from the field maximum near the metallurgical junction. The boundary conditions for the electric field ($\xi(x)$) at the depletion layer edges are given by

$$\xi(-x_1) = 0 \quad \text{and} \quad \xi(x_2) = 0 \quad (7)$$

Similarly, the boundary conditions for normalized difference of hole and electron current density, $P(x) = (J_p(x) - J_n(x))/J_0$ (where $J_0 = J_p + J_n$) at the depletion layer edges, i.e., at $x = -x_1$ and $x = x_2$ are given by

$$P(-x_1) = \left(\frac{2}{M_p} - 1\right) \quad \text{and} \quad P(x_2) = \left(1 - \frac{2}{M_n}\right), \quad (8)$$

where M_n and M_p are the electron and hole multiplication factors whose values are infinitely large of the order

Table 1 Structural and doping parameters

Base material	Sl. no.	f_d (GHz)	W_n (nm)	W_p (nm)	N_D ($\times 10^{23}$ m^{-3})	N_A ($\times 10^{23}$ m^{-3})	N_{n+}, N_{p+} ($\times 10^{26}$ m^{-3})
GaAs	1	60	480.0	480.0	1.000	1.000	1.000
	2	94	320.0	320.0	1.600	1.600	1.000
	3	140	200.0	200.0	3.500	3.500	1.000
	4	220	120.0	120.0	7.500	7.500	1.000
Si	1	94	400.0	380.0	1.200	1.250	1.000
	2	140	280.0	245.0	1.800	2.100	1.000
	3	220	180.0	160.0	3.950	4.590	1.000
	4	300	132.0	112.0	6.000	7.300	1.000
	5	500	72.0	70.0	15.00	16.20	1.000
InP	1	94	350.0	350.0	1.600	1.600	1.000
	2	140	250.0	250.0	2.800	2.800	1.000
	3	220	150.0	151.0	5.000	5.000	1.000
	4	300	110.0	111.0	6.800	6.800	1.000
	5	500	70.0	70.0	13.50	13.50	1.000
	6	1,000	38.0	38.0	27.00	27.00	1.000
4H-SiC	1	94	580.0	580.0	2.800	2.900	1.000
	2	140	400.0	400.0	4.900	5.000	1.000
	3	220	300.0	300.0	6.900	7.000	1.000
	4	300	250.0	250.0	9.500	10.50	1.000
	5	500	160.0	160.0	14.50	16.50	1.000
	6	1,000	90.0	90.0	37.00	43.00	1.000
Wz-GaN	1	94	1,600.0	1,600.0	0.580	0.600	1.000
	2	140	1,100.0	1,100.0	0.680	0.700	1.000
	3	220	735.0	735.0	1.000	1.100	1.000
	4	300	540.0	540.0	1.500	1.600	1.000
	5	500	330.0	330.0	2.800	2.900	1.000
	6	1,000	185.0	185.0	6.800	7.200	1.000
	7	1,500	131.0	131.0	9.800	10.50	1.000
	8	2,000	104.0	104.0	13.50	14.50	1.000
	9	5,000	52.5	52.5	35.50	36.50	1.000

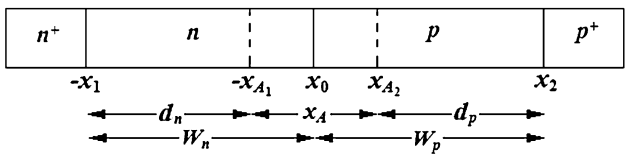

Fig. 1 One-dimensional model of DDR IMPATT device

of $\sim 10^6$ under dark or un-illuminated condition of the device. Electric field profiles ($\xi(x)$ vs. x) and normalized current profiles ($P(x)$ vs. x) are obtained from the DC simulation as mentioned earlier. The breakdown voltage (V_B) and the avalanche zone voltage drop (V_A) are calculated by integrating the spatial field profile ($\xi(x)$ vs. x) over the total depletion layer width (W) and by integrating the spatial field profile over the total avalanche layer width (x_A), respectively, i.e.,

$$V_B = \int_{-x_1}^{x_2} \xi(x)dx \quad \text{and} \quad V_A = \int_{-x_{A_1}}^{x_{A_2}} \xi(x)dx. \tag{9}$$

The DC to RF conversion efficiency is calculated from the semi quantitative formula (Scharfetter and Gummel 1969):

$$\eta(\%) = \frac{2m_p}{\pi} \times \frac{V_D}{V_B} \tag{10}$$

where $V_D = (V_B - V_A)$ = voltage drop across the drift region and $m_p = 1/2$.

Calculation of avalanche response time

The avalanche response time of DDR IMPATTs can be calculated from the knowledge of static spatial distribution of electron and hole ionization rates ($\alpha_n(x)$ vs. x and $\alpha_p(x)$

vs. x) obtained from the DC simulation, saturated drift velocities of charge carriers (v_{sn} and v_{sp}). If τ_{An} and τ_{Ap} are the avalanche response times initiated by electrons and holes, respectively, then these are expressed as (Acharyya and Banerjee 2012, 2013, Acharyya et al. 2012):

$$\tau_{An} = \frac{1}{(v_{sn}+v_{sp})} \int_{-x_{A_1}}^{x_{A_2}} \exp\left[-\int_{-x_{A_1}}^{x} (\alpha_n - \alpha_p)dx'\right] dx, \tag{11}$$

$$\tau_{Ap} = \tau_{An} \exp\left[\int_{-x_{A_1}}^{x_{A_2}} (\alpha_n - \alpha_p)dx\right]. \tag{12}$$

When avalanche process is initiated by a mixture of electrons and holes then the corresponding response time τ_A is given by (Acharyya and Banerjee 2012, 2013, Acharyya et al. 2012)

$$\tau_A = \tau_{An}\left\{(1-k) + k.\exp\left[-\int_{-x_{A_1}}^{x_{A_2}} (\alpha_n - \alpha_p)dx\right]\right\}^{-1} \tag{13}$$

where the parameter $k = J_{ps}/J_s$ and $(1-k) = J_{ns}/J_s$; $J_s = J_{ps} + J_{ns}$ is the total reverse saturation current of the device under dark condition. The expressions for thermally generated electron and hole reverse saturation currents are given by

$$J_{ns} = \left[\frac{qD_n n_i^2}{L_n N_A}\right] \quad \text{and} \quad J_{ps} = \left[\frac{qD_p n_i^2}{L_p N_D}\right]. \tag{14}$$

High-frequency simulation

The magnitude of peak field at the junction (ξ_p), the widths of avalanche and drift zones (x_A and x_D; where $x_D = d_n + d_p$) and the voltage drops across these zones (V_A, V_D) are obtained from the DC simulation program. These values are fed back as input parameters in the high-frequency simulation program. The depletion layer edges of the device are obtained from the output of DC simulation program. The edges of the depletion layer are then taken as the starting and end points of high-frequency simulation program. Two second-order differential equations are framed from Gummel–Blue model (Roy et al. 1985) by resolving the device impedance $Z(x,\omega)$ into its real part $R(x,\omega)$ and imaginary part $X(x,\omega)$; where $Z(x,\omega) = R(x,\omega) + jX(x,\omega)$. Two simultaneous second-order differential equations in R and X are numerically solved using Runge–Kutta method (Roy et al. 1985). Double-iteration over the initial choice of the values of R and X at one edge is carried out till the boundary conditions for R and X are satisfied at the other edge (Acharyya and Banerjee 2012; Roy et al. 1985). The negative specific resistance ($R(x)$ vs. x) and specific reactance ($X(x)$ vs. x) profiles in the depletion layer of the device are obtained from the above-mentioned solution. The device negative resistance (Z_R) and reactance (Z_X) are obtained from the numerical integration of the respective $R(x)$- and $X(x)$-profiles over the depletion layer width (W), i.e.,

$$Z_R = \int_{-x_1}^{x_2} R(x)dx \quad \text{and} \quad Z_X = \int_{-x_1}^{x_2} X(x)dx. \tag{15}$$

The device impedance is given by $Z_D = Z_R + jZ_X$, while the device admittance is $Y_D = Z_D^{-1} = G + jB$. The negative conductance (G) and positive susceptance (B) of the device at a particular frequency are computed from the following expressions:

$$|G(\omega)| = \frac{Z_R}{(Z_R^2 + Z_X^2)} \quad \text{and} \quad |B(\omega)| = \frac{-Z_X}{(Z_R^2 + Z_X^2)}. \tag{16}$$

It may be noted that both G and B are normalized with respect to the effective junction area (A_j) of the device. The admittance characteristics, i.e., $G(\omega)$ versus $B(\omega)$ plots of the device are obtained from the above analysis for different bias current densities. The avalanche resonance frequency (f_a) at which the susceptance (B) changes its sign from positive to negative, i.e., from inductive to capacitive is also obtained from the admittance plots. The RF power output P_{RF} from the device can be obtained from the following expression:

$$P_{RF} = \frac{1}{2}(V_{RF})^2 |G_p| A_j, \tag{17}$$

where V_{RF} is the RF voltage ($V_{RF} = m_x \times V_B$; where the modulation index, $m_x \leq 30$ % under small-signal condition; whereas m_x is taken as 25 % in the calculations presented in this paper), $|G_p|$ is the peak magnitude of the negative conductance at peak optimum frequency (f_p) and A_j is the effective junction area of the device ($A_j = \pi(D_j/2)^2$, and D_j is the effective junction diameter of the device (assuming the circular cross-section of the device)).

In the "Results and discussion" section, the DC and high-frequency results of DDR IMPATT devices based on different semiconductors are presented and discussed in detail. The numerical simulation approach described briefly in this section is verified by the authors by comparing the simulation obtained results of Si, GaAs and InP DDR IMPATTs presented in this paper at different mm-wave frequencies with published experimental reports. So far as authors' knowledge is concerned no experimental report on 4H-SiC and Wz-GaN DDR IMPATTs is available in published literature within the mm-wave and THz frequency range under consideration. That is way the simulation predicted results of 4H-SiC and Wz-GaN DDR IMPATTs could not be verified.

Table 2 DC properties

Base material	Sl. no.	J_0 ($\times 10^8$ Am^{-2})	ξ_p ($\times 10^7$ V m^{-1})	V_B (V)	V_A (V)	η (%)	x_A (nm)	x_A/W (%)
GaAs	1	2.20	5.6067	28.87	17.06	13.02	376.0	40.00
	2	5.60	6.0442	22.67	15.57	9.97	332.0	55.33
	3	11.50	7.3067	15.78	11.41	8.82	208.0	54.74
	4	24.50	9.1317	11.61	9.49	5.77	146.0	66.36
Si	1	3.40	6.0115	24.27	16.21	10.58	352.0	46.32
	2	5.80	6.6617	18.98	13.52	9.16	268.0	53.07
	3	13.0	8.1990	13.74	10.29	7.99	170.0	53.10
	4	17.2	9.3490	11.29	9.07	6.25	134.0	59.82
	5	52.0	12.1760	9.06	7.75	4.59	90.0	67.16
InP	1	1.40	7.3904	28.82	14.42	15.90	230.0	33.72
	2	2.90	7.9279	19.78	10.44	15.02	156.0	33.91
	3	5.00	8.5904	13.30	7.48	13.93	104.0	37.01
	4	7.80	8.9205	10.71	6.29	13.13	84.0	41.79
	5	19.0	9.7447	7.08	4.56	11.35	56.0	46.67
	6	40.5	10.6450	4.43	3.34	7.82	38.0	67.85
4H-SiC	1	4.00	35.9060	226.08	111.09	16.19	382.0	33.81
	2	9.00	38.9163	158.19	79.82	15.77	252.0	32.31
	3	21.0	40.6251	121.47	69.46	14.62	212.0	36.55
	4	51.0	42.6311	107.72	60.73	13.89	178.0	37.08
	5	135.0	45.2179	86.32	53.26	12.19	152.0	50.67
	6	460.0	51.7022	51.54	36.35	9.38	92.0	61.33
Wz-GaN	1	0.05	15.9820	251.61	123.12	16.25	904.0	28.43
	2	0.30	16.2877	215.59	106.21	16.15	758.0	35.09
	3	1.00	17.0345	155.13	81.57	15.49	560.0	39.16
	4	1.50	17.8712	118.13	62.21	15.07	408.0	38.49
	5	3.00	19.2765	76.34	41.42	14.56	252.0	39.38
	6	10.8	21.4739	41.76	24.28	13.32	134.0	40.61
	7	16.0	22.4766	31.43	19.31	12.27	102.0	45.95
	8	23.5	23.3778	25.21	16.13	11.46	82.0	48.81
	9	30.0	26.3812	11.92	9.72	5.88	44.0	67.69

Results and discussion

The active layer widths (W_n, W_p) and background doping concentrations (N_D, N_A) of DDR IMPATT devices (Table 1) based on different semiconductor materials have been designed to operate at different mm-wave and terahertz frequencies using simple transit time formula (Sze and Ryder 1971) and simulated using DC (Acharyya and Banerjee 2012; Roy et al. 1979) and high-frequency (Acharyya and Banerjee 2012; Roy et al. 1985) simulation techniques as described briefly in the previous section.

DC properties

Important DC parameters such as peak electric field (ξ_p), breakdown voltage (V_B), avalanche zone voltage (V_A), DC to RF conversion efficiency (η), avalanche layer width (x_A) and ratio of avalanche zone width to total depletion layer width (x_A/W) of the designed DDR IMPATTs are obtained from DC simulation and given in Table 2. Variations of ξ_p, V_B and η with operating frequency of GaAs and Si-based DDR IMPATTs are shown in Fig. 2. Variations of the above parameters (ξ_p and V_B, η) of InP, 4H-SiC and Wz-GaN-based DDR IMPATTs with operating frequency are shown in Figs. 3, 4. Thus, a comparison of the DC properties of DDR IMPATTs based on different semiconductors can be made from Table 2 and Figs. 2, 3, 4 at different operating frequencies. Table 2 shows that peak electric field (ξ_p) increases while the breakdown voltage (V_B), avalanche zone voltage (V_A), DC to RF conversion efficiency (η) and avalanche layer width (x_A) decrease in the DDR IMPATTs based on different materials as the operating frequency increases. Peak electric field (ξ_p) is highest in 4H-SiC based DDRs among all other DDR IMPATTs under consideration at any operating frequency; it increases from 3.59×10^8 to 5.17×10^8 V m^{-1} as the operating

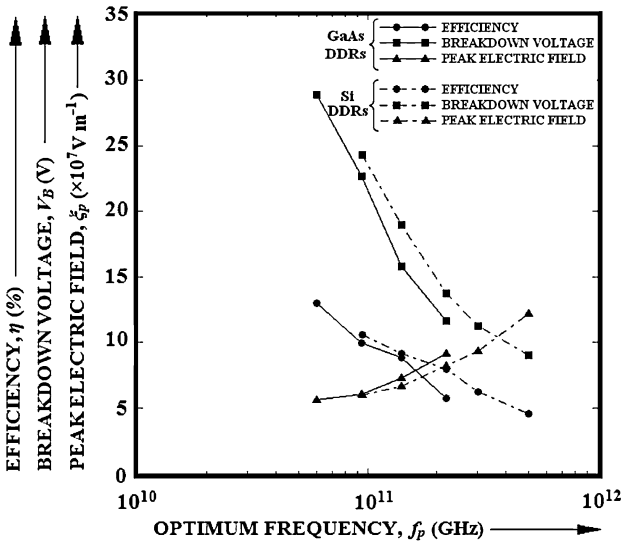

Fig. 2 Variations of DC to RF conversion efficiency, breakdown voltage and peak electric field with optimum frequency of GaAs and Si-based DDR IMPATTs

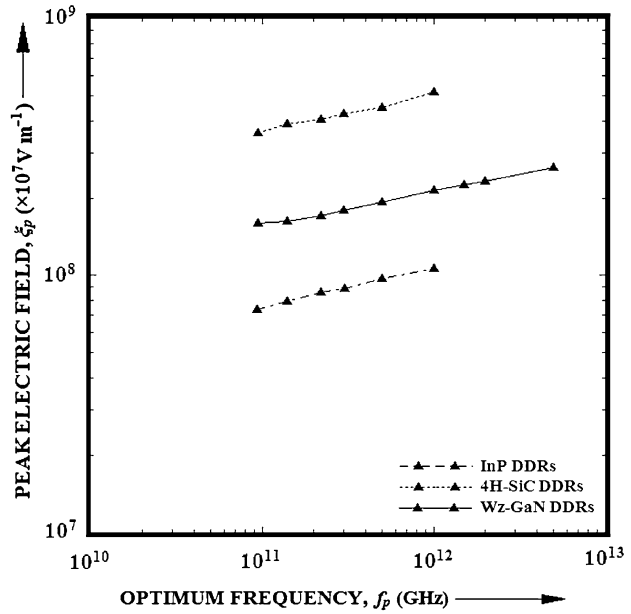

Fig. 3 Variation of peak electric field with optimum frequency of InP, 4H-SiC and Wz-GaN based DDR IMPATTs

frequency increases from 94 GHz to 1.0 THz. In Wz-GaN based DDR IMPATTs, ξ_p is of the same order ($\sim 10^8$ V m^{-1}) but lower than 4H-SiC DDRs. Peak electric fields (ξ_p) of GaAs, Si and InP-based DDR IMPATTs are one order lower ($\sim 10^7$ V m^{-1}) as compared with 4H-SiC and Wz-GaN based DDR IMPATTs. But among GaAs, Si and InP-based DDR IMPATTs, the peak field is highest in InP IMPATTs followed by Si and GaAs IMPATTs. Figure 4 and Table 2 show that the breakdown voltage (V_B) of

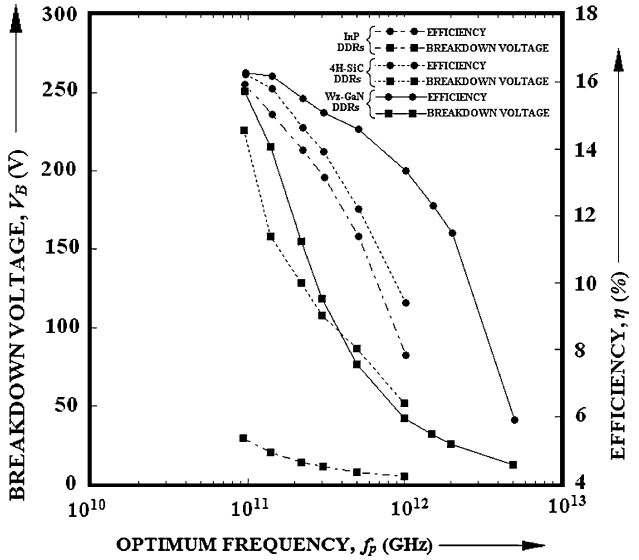

Fig. 4 Variations of DC to RF conversion efficiency and breakdown voltage with optimum frequency of InP, 4H-SiC and Wz-GaN based DDR IMPATTs

Wz-GaN based DDR IMPATTs is highest among all other semiconductor-based DDR devices up to 0.3 THz beyond which the breakdown voltage (V_B) of 4H-SiC based IMPATTs exceeds that of Wz-GaN based IMPATTs. It is observed that GaAs, Si and InP-based DDRs have lower breakdown voltage (V_B) than either 4H-SiC or Wz-GaN based DDRs. It is observed from Table 2 as well as Figs. 2 and 4 that breakdown voltage (V_B) of InP DDR device is highest among GaAs, Si and InP DDRs at the same operating frequencies. From the knowledge of avalanche zone voltage (V_A) and breakdown voltage (V_B), the drift zone voltage drop ($V_D = V_B - V_A$) of the device can be calculated. The ratio of drift zone voltage to breakdown voltage (V_D/V_B) decreases in all the devices under consideration as the operating frequency increases. The ratio V_D/V_B is much higher in Wz-GaN DDRs (0.510 at 94 GHz, 0.419 at 1.0 THz) and 4H-SiC DDRs (0.509 at 94 GHz, 0.295 at 1.0 THz) as compared with GaAs DDRs (0.313 at 94 GHz, 0.183 at 220 GHz) or Si DDRs (0.332 at 94 GHz, 0.145 at 0.5 THz) and InP DDRs (0.489 at 94 GHz, 0.246 at 1.0 THz). The magnitudes of V_D/V_B in Wz-GaN, 4H-SiC and InP DDRs are comparable up to lower mm-wave frequencies. At higher frequencies the ratio V_D/V_B decreases sharply in 4H-SiC and InP DDRs. It may be noted that the rate of decrease of V_D/V_B with respect to frequency is much less in Wz-GaN based DDR IMPATTs. The ratio V_D/V_B is nearly same in GaAs and Si DDRs up to some limiting frequency beyond which V_D/V_B is higher in Si DDRs. According to the semi-quantitative formula of DC to RF conversion efficiency ($\eta = (1/\pi) \times (V_D/V_B)$) (Scharfetter and Gummel 1969) the DC to RF conversion efficiency (η)

of IMPATT devices is directly proportional to the ratio V_D/V_B. Thus, the variation of DC to RF conversion efficiency (η) of the devices with frequency exhibits the same nature as that of V_D/V_B. Figure 4 and Table 2 show that the DC to RF conversion efficiencies (η) of InP, 4H-SiC and Wz-GaN DDRs are comparable and much greater than DC to RF conversion efficiencies (η) of GaAs and Si DDRs as shown in Fig. 2 and Table 2. DC to RF conversion efficiency (η) is highest in Wz-GaN DDRs and rate of decrease of η with respect to operating frequency ($d\eta/df$) is also much lower (Fig. 4) in Wz-GaN DDRs than that in InP and 4H-SiC DDRs up to 1.0 THz.

The ratio of avalanche zone width to total drift layer width (x_A/W) for all the devices under consideration increases sharply at higher operating frequencies. Higher x_A/W indicates wider avalanche zone, which leads to higher avalanche voltage (V_A) and lower drift zone voltage (V_D). The lower the V_D/V_B, the lower the efficiency (η). Thus, the rapid widening of avalanche region at higher operating frequencies is the primary cause of sharp decrease of η at higher operating frequencies. In case of GaA-based DDRs x_A/W is 40.0 % at 60 GHz but it rises to 66.36 % at 220 GHz which causes sharp decrease of η at 220 GHz frequency. But in Si DDRs at 220 GHz, x_A/W is 53.10 %, but it rises to 67.16 % at 500 GHz and this leads to sharp fall in η at higher mm-wave and THz frequencies. In case of InP, 4H-SiC and Wz-GaN DDR devices the magnitude of x_A/W is much lower up to a frequency of 0.3 THz (41.79 % in InP DDR, 37.08 % in 4H-SiC DDR, 38.39 % in Wz-GaN), but it increases rapidly above 0.3 THz in InP and 4H-SiC DDRs and becomes 67.85 and 61.83 % at 1.0 THz, respectively. This leads to very low value of η (7.82 and 9.38 % respectively) for InP and 4H-SiC DDRs at that frequency. But in Wz-GaN DDRs, sharp rise in x_A/W is observed at frequencies above 1.0 THz whose magnitude increases up to 67.69 % at 5.0 THz leading to very low efficiency (5.58 %) of Wz-GaN DDRs at that frequency.

Avalanche response times

Avalanche response times (τ_A) of the DDR IMPATTs based on different semiconductors are calculated by Eq. (13). Spatial variations of ionization rates of electrons (α_n) and holes (α_p) for each device are obtained from the output of the DC program and used to solve Eqs. (11) and (13). Transit times (τ_T) associated with the DDR IMPATT devices based on GaAs, Si, InP, 4H-SiC and Wz-GaN operating at different mm-wave and THz frequencies are obtained from transit time formula of Sze and Ryder (1971). The computed values of τ_A and τ_T of all DDR devices under consideration are given in Table 3. Figures 5 and 6 show the variations of τ_A and τ_T with operating frequency in GaAs, Si-based DDRs and InP, 4H-SiC, Wz-GaN based DDRs, respectively. DDR IMPATTs based on a particular semiconductor can be operated at higher frequencies provided the avalanche response time (τ_A) is much lower than the transit time (τ_T) of carriers at the higher frequencies (Acharyya and Banerjee 2012, 2013). Avalanche response time (τ_A) of the device depends on the saturated drift velocities and ionization rates of electron and holes (v_{sn}, v_{sp} and α_n, α_p, respectively) of the base semiconductor. Thus, the type of the base material determines the value of τ_A at a particular frequency. Figure 5 and Table 3 show that τ_A of GaAs DDRs is higher than that of Si DDRs (at 94 GHz τ_A of GaAs DDR is 1.72 times higher than τ_A of Si DDR; whereas at 220 GHz this ratio is 2.15). That is why DDR IMPATTs based on Si can operate at much higher frequencies (up to 0.5 THz) than those based on GaAs (up to 220 GHz). It is observed from

Table 3 Avalanche response times and transit times

Base material	Sl. no.	f_d (GHz)	τ_A (Sec)	τ_T (Sec)
GaAs	1	60	3.660131×10^{-12}	1.920000×10^{-11}
	2	94	3.328758×10^{-12}	1.280000×10^{-11}
	3	140	3.113022×10^{-12}	0.800000×10^{-11}
	4	220	3.041175×10^{-12}	0.480000×10^{-11}
Si	1	94	1.940812×10^{-12}	1.244168×10^{-11}
	2	140	1.667003×10^{-12}	0.870917×10^{-11}
	3	220	1.417097×10^{-12}	0.559875×10^{-11}
	4	300	1.268324×10^{-12}	0.041057×10^{-11}
	5	500	1.191345×10^{-12}	0.223950×10^{-11}
InP	1	94	3.771131×10^{-13}	1.116667×10^{-11}
	2	140	2.271644×10^{-13}	0.833333×10^{-11}
	3	220	1.727141×10^{-13}	0.500000×10^{-11}
	4	300	1.474539×10^{-13}	0.366667×10^{-11}
	5	500	0.914383×10^{-13}	0.233333×10^{-11}
	6	1,000	0.733187×10^{-13}	0.126667×10^{-11}
4H-SiC	1	94	2.361382×10^{-15}	0.547169×10^{-11}
	2	140	1.524503×10^{-15}	0.377358×10^{-11}
	3	220	1.248335×10^{-15}	0.283018×10^{-11}
	4	300	1.029931×10^{-15}	0.235849×10^{-11}
	5	500	0.800814×10^{-15}	0.150943×10^{-11}
	6	1,000	0.628814×10^{-15}	0.094339×10^{-11}
Wz-GaN	1	94	3.462981×10^{-16}	1.066667×10^{-11}
	2	140	2.729583×10^{-16}	0.733333×10^{-11}
	3	220	1.759941×10^{-16}	0.490000×10^{-11}
	4	300	1.110175×10^{-16}	0.360000×10^{-11}
	5	500	0.547288×10^{-16}	0.220000×10^{-11}
	6	1,000	0.207058×10^{-16}	0.123333×10^{-11}
	7	1,500	0.134709×10^{-16}	0.087333×10^{-11}
	8	2,000	0.104014×10^{-16}	0.069333×10^{-11}
	9	5,000	0.099169×10^{-16}	0.035000×10^{-11}

Table 3 that the values of τ_A of InP, 4H-SiC and Wz-GaN DDRs are lower than those of GaAs and Si DDRs. Further from Fig. 6 and Table 3, it is observed that τ_A of Wz-GaN DDR IMPATTs is much smaller than that of InP DDR IMPATTs. At 94 GHz, τ_A of Wz-GaN DDR is 9.18×10^{-4} times of InP DDR and τ_A of 4H-SiC DDR is 6.26×10^{-3} times of InP DDR at the same frequency, whereas the same ratio of τ_A of Wz-GaN DDR to τ_A of InP and 4H-SiC DDRs become 2.82×10^{-4} and 8.58×10^{-3}, respectively, at 1.0 THz. It therefore turns out that τ_A of Wz-GaN DDRs is the lowest of all other DDR IMPATTs under consideration (at 94 GHz τ_A of Wz-GaN DDR is 0.15 times than that of 4H-SiC DDR, whereas at 1.0 THz this ratio becomes 0.33). Due to very small avalanche response time (τ_A), of the order of $\sim 10^{-16}$ s, Wz-GaN DDR IMPATT device is capable of operating up to 5.0 THz, whereas the highest operating frequencies of GaAs, Si, InP and 4H-SiC DDRs are limited to 220 GHz, 500 GHz, 1.0 THz and 1.0 THz, respectively.

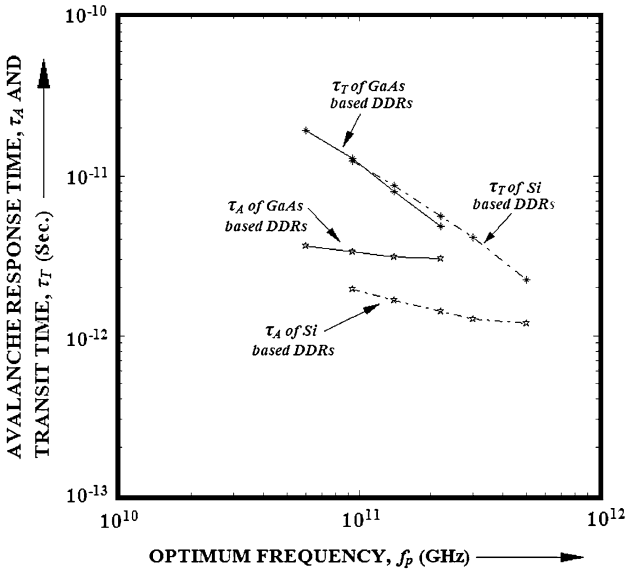

Fig. 5 Variations of avalanche response time and transit time with optimum frequency of GaAs and Si-based DDR IMPATTs

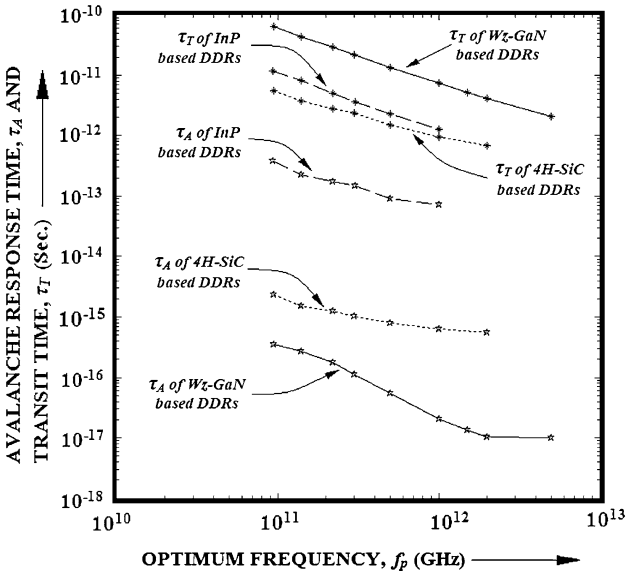

Fig. 6 Variations of avalanche response time and transit time with optimum frequency of InP, 4H-SiC and Wz-GaN based DDR IMPATTs

High-frequency properties

The important high-frequency parameters obtained from this analysis are optimum frequency (f_p), peak negative conductance (G_p), corresponding susceptance (B_p), quality factor or Q-factor (Q_p), negative resistance (Z_R) and RF power output (P_{RF}). Those parameters are obtained from the high-frequency simulation of GaAs, Si, InP, 4H-SiC and Wz-GaN DDR IMPATTs and listed in Table 4. Admittance characteristics or high-frequency conductance-susceptance plots of GaAs and Si DDRs are shown in Fig. 7 while those of InP and 4H-SiC DDRs are shown in Figs. 8 and 9, respectively, and those of Wz-GaN DDRs are shown in Figs. 10 and 11, respectively. It is observed from Table 4 and Figs. 7, 8, 9, 10, 11 that the magnitudes of G_p and B_p increase with the increase of operating frequency. Q-factor ($Q_p = -B_p/G_p$) of the device determines the growth rate of IMPATT oscillation. Lower Q-factor close to $Q_p \approx 1$ suggests higher oscillation growth rate. It is observed from Table 4 that the Q-factors of 4H-SiC DDRs are lowest ($Q_p < 1$) from 94 GHz to 1.0 THz of all other DDRs under consideration. It is interesting to note that Q-factor (Q_p) of GaAs, Si and InP DDRs increases with the increase of operating frequency, but Q-factor (Q_p) of Wz-GaN DDR IMPATTs decreases with the increase of operating frequency. This fact suggests that the oscillation growth rate improves in Wz-GaN based DDRs at higher frequencies (up to 5.0 THz).

Negative resistances (Z_R) of the devices are calculated from Eq. (15) and given in Table 4. Table 4 shows that, the magnitude of negative resistance (Z_R) of DDR IMPATTs based on GaAs, Si, InP, 4H-SiC and Wz-GaN decreases with the increase of operating frequency. It is interesting to observe that the magnitude of Z_R is highest in 4H-SiC based DDRs among all other devices from 94 GHz to 1.0 THz. Higher magnitude of negative resistance implies that higher RF power output can be obtained from the 4H-SiC based DDR IMPATT devices in comparison with GaAs, Si, InP and Wz-GaN based DDR IMPATT devices operating at same frequency.

RF power outputs (P_{RF}) of the DDR IMPATT devices under consideration at different operating frequencies are obtained from Eq. (17) from the knowledge of breakdown

Table 4 High-frequency properties

Base material	Sl. no.	f_p (GHz)	G_p ($\times 10^7$ Sm^{-2})	B_p ($\times 10^7$ Sm^{-2})	$Q_p = -(B_p/G_p)$	Z_R ($\times 10^{-9}$ Ωm^{-2})	P_{RF} (mW)	D_j (μm)
GaAs	1	60	−2.9548	3.5293	1.19	−13.9461	1828.47	55.0
	2	94	−5.8886	7.8662	1.34	−6.0988	909.89	35.0
	3	140	−10.4730	19.4641	1.86	−2.1438	400.04	25.0
	4	220	−17.1452	56.7970	3.31	−0.4871	226.89	20.0
Si	1	94	−4.0002	6.5654	1.64	−6.7679	708.43	35.0
	2	140	−8.0772	15.4697	1.92	−2.6524	446.35	25.0
	3	219	−18.0334	38.7885	2.15	−0.9855	334.23	20.0
	4	302	−26.2239	80.1598	3.05	−0.3686	184.59	15.0
	5	500	−67.5571	222.3756	3.29	−0.1251	136.10	10.0
InP	1	94	−8.2457	6.8436	0.83	−7.1811	2059.17	35.0
	2	140	−26.6945	13.7556	0.52	−2.9599	1602.12	25.0
	3	220	−49.3589	47.2443	0.96	−1.0573	857.17	20.0
	4	300	−78.9689	72.7609	0.92	−0.6849	500.22	15.0
	5	501	−278.1512	213.6971	0.77	−0.2268	342.21	10.0
	6	1,000	−598.7561	703.7719	1.17	−0.0701	72.10	5.0
4H-SiC	1	95	−1.9711	0.5574	0.28	−46.9756	30,290.98	35.0
	2	140	−4.2152	1.3511	0.32	−21.5132	16,180.81	25.0
	3	220	−9.1919	3.7236	0.41	−9.3454	13,315.09	20.0
	4	300	−20.4917	8.3277	0.41	−4.1883	13,130.85	15.0
	5	500	−51.1584	14.3506	0.28	−1.8121	9,355.78	10.0
	6	1,000	−121.6192	46.1491	0.38	−0.7187	1,982.31	5.0
Wz-GaN	1	95	−0.1638	1.7788	10.86	−5.1361	3,117.78	35.0
	2	140	−0.3953	3.7869	9.58	−2.7262	2,818.41	25.0
	3	220	−1.1101	9.1187	8.21	−1.3155	2,622.73	20.0
	4	300	−2.3439	16.9007	7.21	−0.8051	1,806.27	15.0
	5	500	−8.1282	46.6598	5.74	−0.3632	1,162.62	10.0
	6	1,000	−47.1109	180.2237	3.82	−0.1358	504.16	5.0
	7	1,500	−126.7654	408.2341	3.22	−0.0693	192.09	2.5
	8	2,000	−211.6412	730.3715	3.45	−0.0366	47.54	1.2
	9	5,000	−445.7865	1,045.0674	2.34	−0.0345	7.62	0.7

voltage (V_B), voltage modulation factor ($m_x = 25$ %), magnitude of peak negative conductance (G_p) and effective junction area of the device (A_j). The effective junction diameter (D_j) is scaled down from 55 to 0.7 μm as the frequency of operation increases from 60 GHz to 5.0 THz through a rigorous thermal analysis (Acharyya et al. 2011, 2010) in continuous-wave (CW) mode considering proper heat sinking aspects which is sufficient to avoid the thermal runway and burn out of the device and corresponding D_j values are given in Table 4. Variation of RF power output (P_{RF}) with optimum frequency of GaAs, Si, InP, 4H-SiC and Wz-GaN-based DDR IMPATTs is shown in Fig. 12. Figure 12 and Table 4 show that P_{RF} decreases as the operating frequency of the device increases. It is interesting to observe from Fig. 12 and Table 4 that RF power output (P_{RF}) of GaAs and Si-based DDR IMPATTs is almost comparable up to 220 GHz; up to 94 GHz, GaAs DDRs can deliver marginally higher power output as compared with Si DDRs, but above 94 GHz Si DDRs exceed GaAs DDRs as regards P_{RF}. It is also observed that InP-based DDR IMPATTs are capable of delivering higher output power as compared with DDR IMPATTs based on GaAs and Si. Another advantage of InP DDR IMPATTs is that the device can operate up to much higher frequencies (up to 1.0 THz), whereas the high-frequency performance of GaAs and Si DDR IMPATTs are limited to 220 GHz and 0.5 THz, respectively. It is interesting to note that Wz-GaN and 4H-SiC DDR IMPATTs are potential candidates for THz operation due to their higher RF power outputs at THz frequencies. Up to 1.0 THz 4H-SiC IMPATTs provide the highest RF power output among all other devices under consideration. But the genuine advantage of Wz-GaN DDR IMPATTs is that it can operate up to 5.0 THz with appreciable power output.

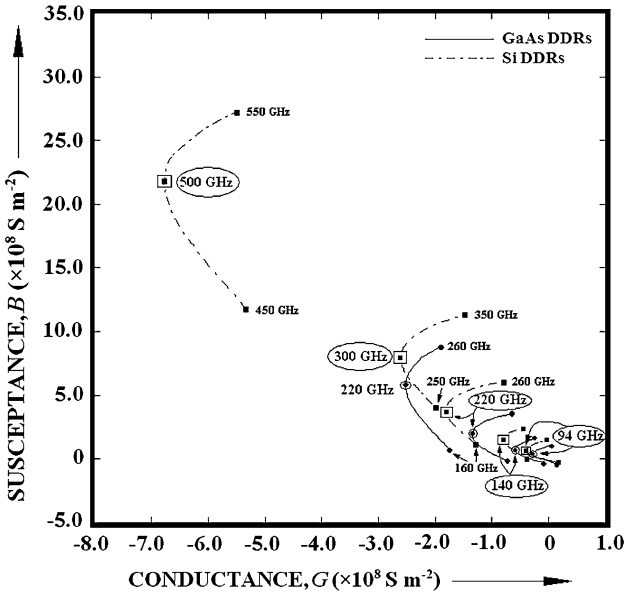

Fig. 7 Admittance characteristics of GaAs and Si-based DDR IMPATTs

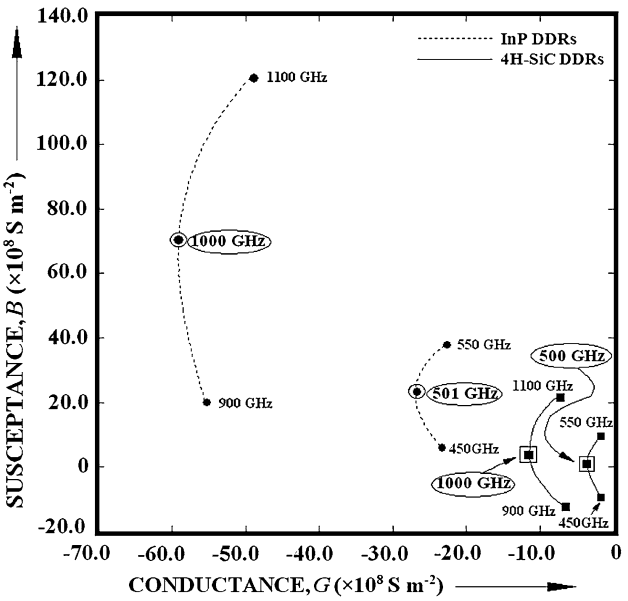

Fig. 9 Admittance characteristics of 0.5, 1.0 THz InP and 4H-SiC based DDR IMPATTs

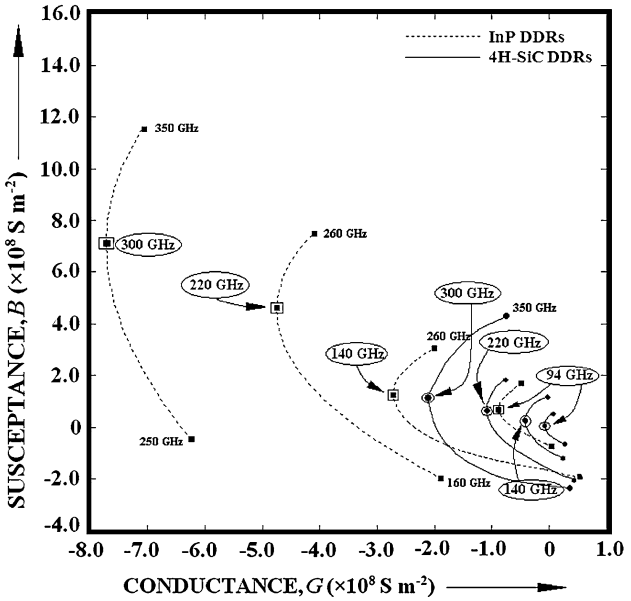

Fig. 8 Admittance characteristics of 94, 140, 220 GHz, 0.3 THz InP and 4H-SiC based DDR IMPATTs

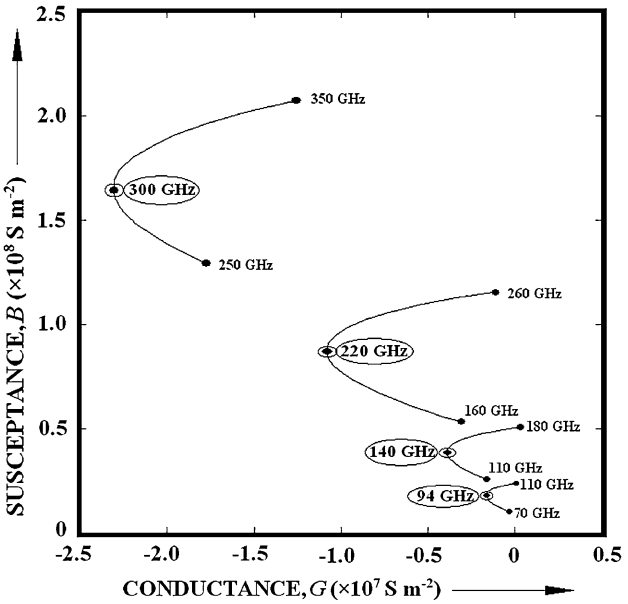

Fig. 10 Admittance characteristics of 94, 140, 220 GHz, 0.3 THz Wz-GaN based DDR IMPATTs

Validation of the simulation results

Experimentally obtained RF power output from Si DDR IMPATT sources are 600 mW at 94 GHz (Luy et al. 1987) and 300 mW at 140 GHz (Wollitzer et al. 1996) which are shown in Fig. 12. Figure 12 shows that the experimental results are in very close agreement with the simulation results for Si DDR IMPATTs which validates the DC and high-frequency simulation technique adopted by the authors and used in this paper. Experimentally obtained RF power output from GaAs DDR IMPATT sources are 1.24 W, 270 and 100 mW at 60, 95 and 144 GHz, respectively (Adlerstein and Chu 1984; Eisele 1989; Tschernitz and Freyer 1995), and the same from InP DDR IMPATT source is 55 mW at 84.8 GHz (Eisele et al. 1996). Experimentally obtained power outputs from GaAs and InP IMPATT sources are also shown in Fig. 12. It can be observed from Fig. 12 that at 60 GHz the simulated and experimental results for GaAs DDR IMPATT source are in

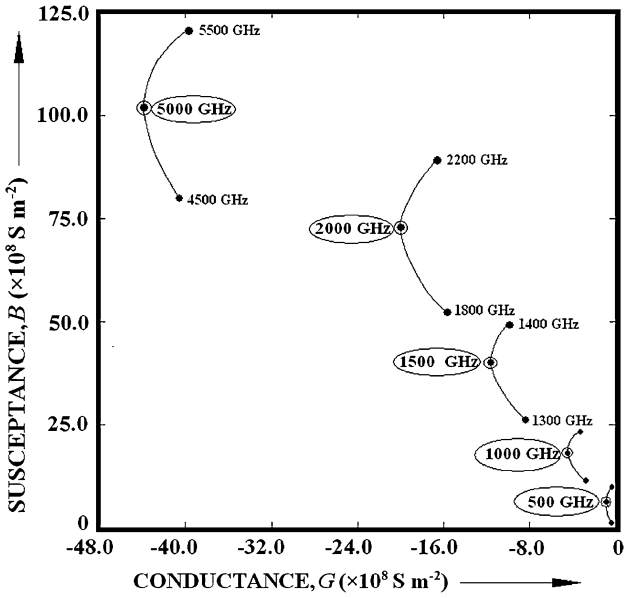

Fig. 11 Admittance characteristics of 0.5, 1.0, 1.5, 2.0, 5.0 THz Wz-GaN based DDR IMPATTs

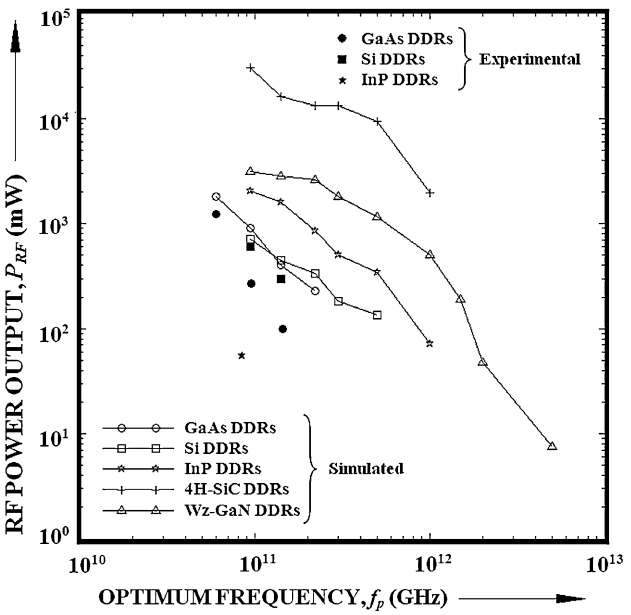

Fig. 12 Variation of RF power output with optimum frequency of GaAs, Si, InP, 4H-SiC and Wz-GaN based DDR IMPATTs

close agreement; but above 60 GHz simulation results are predicting much higher power output as compared with the experimentally obtained values. Similarly, at W-band (75–110 GHz) simulation predicted RF power out is much higher as compared with the experimentally obtained value for InP DDR IMPATT source. Lack of mature fabrication technology of GaAs and InP-based DDR IMPATT devices higher mm-wave frequency bands and lack of optimized design of the devices used for those experiments may be the cause of getting lower power outputs experimentally. But so far as the authors' knowledge is concerned, no experimental report on 4H-SiC and Wz-GaN based DDR IMPATT source operating at mm-wave or THz frequency bands is available in published literatures. That is why the simulation results of 4H-SiC and Wz-GaN based DDR IMPATTs presented in this paper could not be compared with experimentally obtained results.

Conclusions

Millimeter-wave and Terahertz performance of DDR IMPATT devices based on GaAs, Si, InP, 4H-SiC and Wz-GaN are investigated in this paper. High-frequency limitations of DDR IMPATTs based on the above-mentioned semiconductors are studied from the avalanche response time of the devices operating at mm-wave and THz frequencies. Wz-GaN DDR IMPATTs emerge as the most suitable material for generation of THz frequencies up to 5.0 THz due to their small avalanche response time, high DC to RF conversion efficiency and sufficiently high RF power output of Wz-GaN based DDRs at THz frequencies. But up to 1.0 THz, 4H-SiC DDR IMPATTs excel Wz-GaN DDR IMPATTs due to their higher power output. It may therefore be concluded that Wz-GaN and 4H-SiC are highly suitable semiconductors for IMPATT action in both mm-wave and THz frequency ranges with respect to power output and efficiency. The simulation results and corresponding designs would be useful for undertaking an experimental program to fabricate the THz 4H-SiC and Wz-GaN IMPATTs using MBE or metallo-organic chemical vapor deposition techniques.

References

Acharyya A, Banerjee JP (2012) Analysis of photo-irradiated double-drift region silicon impact avalanche transit time devices in the millimeter-wave and terahertz regime. Terahertz Sci Technol 5:97–113

Acharyya A, Banerjee JP (2013) Potentiality of IMPATT devices as terahertz source: an avalanche response time based approach to determine the upper cut-off frequency limits. IETE J Res 59 (Accepted)

Acharyya A, Pal B, Banerjee JP (2010) Temperature distribution inside semi-infinite heat sinks for IMPATT sources. Int J Eng Sci Technol 2:5142–5149

Acharyya A, Mukherjee J, Mukherjee M, Banerjee JP (2011) Heat sink design for IMPATT diode sources with different base materials operating at 94 GHz. Arch Phys Res 2:107–126

Acharyya A, Banerjee S, Banerjee JP (2012) Calculation of avalanche response time for determining the high frequency performance limitations of IMPATT devices. J Electron Dev 12:756–760

Adlerstein MG, Chu SLG (1984) GaAs IMPATT diodes for 60 GHz. IEEE Electron Devices Lett 5:97–98

Banerjee S, Mukherjee M, Banerjee JP (2010) Bias current optimization of Wurtzite-GaN DDR IMPATT diode for high power operation at THz frequencies. Int J Adv Sci Technol 16:12–20

Canali C, Ottaviani G, Quaranta AA (1971) Drift velocity of electrons and holes and associated anisotropic effects in silicon. J Phys Chem Solids 32:1707

Chang Y, Hellum JM, Paul JA, Weller KP (1977) Millimeter-wave IMPATT sources for communication applications. In: IEEE MTT-S international microwave symposium digest, pp 216–219

Crowe TW, Hesler JL, Retzloff SA, Pouzou C, Schoenthal GS (2011a) Solid state lo sources for greater than 2THz. 2011 ISSTT Digest. In: 22nd symposium on space terahertz technology, Tucson, AZ, USA

Crowe TW, Hesler JL, Retzloff SA, Pouzou C, Hester JL (2011b) Multiplier based sources for frequencies above 2 THz. In: 36th international conference on infrared, millimeter and terahertz sources (IRMMW-THz), p 1

Dalle C, Rolland P, Lieti G (1990) Flat doping profile double-drift silicon IMPATT for reliable CW high power high-efficiency generation in the 94-GHz window. IEEE Trans Electron Devices 37:227–236

Debus C, Bolivar PH (2007) Frequency selective surfaces for high sensitivity terahertz sensing. Appl Phys Lett 91:184102

Eisele H (1989) Selective etching technology for 94 GHz GaAs IMPATT diodes on diamond heat sinks. Solid-State Electronics 32:253–257

Eisele H, Haddad GI (1995) GaAs TUNNETT diodes on diamond heat sinks for 100 GHz and above. IEEE Trans Microwave Theory Tech 43:210–213

Eisele H, Chen CC, Munns GO, Haddad GI (1996) The potential of InP IMPATT diodes as high-power millimeter-wave sources: first experimental results. IEEE MTT-S Int Microwave Symp Digest 2:529–532

Electronic Archive (2012) New Semiconductor Materials, Characteristics and Properties. http://www.ioffe.ru/SVA/NSM/Semicond

Fitzgerald AJ, Cole BE, Taday PF (2005) Nondestructive analysis of tablet coating thicknesses using terahertz pulsed imaging. J Pharm Sci 94:177–183

Grant WN (1973) Electron and hole ionization rates in epitaxial Silicon. Solid State Electron 16:1189–1203

Gray WW, Kikushima L, Morentc NP, Wagner RJ (1969) Applying IMPATT power sources to modern microwave systems. IEEE J Solid-State Circuits 4:409–413

Grischkowsky D, Keiding S, Exter M, Fattinger C (1990) Far-infrared time-domain spectroscopy with terahertz beams of dielectrics and semiconductors. J Opt Soc Am B 7:2006–2015

Gummel HK, Blue JL (1967) A small-signal theory of avalanche noise in IMPATT diodes. IEEE Trans Electron Dev 14:569–580

Heyminck S, Güsten R, Graf U, Stutzki J, Hartogh P, Hübers HW, Ricken O, Klein B (2009) GREAT: ready for early science aboard SOFIA. In: Proceedings of 20th international symposium on space terahertz technology, Charlottesville, VA, pp 315–317

Ito M, Kagawa S, Kaneda T, Yamaoka T (1978) Ionization rates for electrons and holes in GaAs. J Appl Phys 49:4607

Jördens C, Koch M (2008) Detection of foreign bodies in chocolate with pulsed terahertz spectroscopy. Opt Eng 47:037003

Kao CW, Crowell CR (1980) Impact ionization by electrons and holes in InP. Solid State Electron 23:881–891

Konstantinov AO, Wahab Q, Nordell N, Lindefelt U (1997) Ionization rates and critical fields in 4H-Silicon Carbide. Appl Phys Lett 71:90–92

Kramer B, Micrea A (1975) Determination of saturated electron velocity in GaAs. Appl Phys Lett 26:623–624

Kunihiro K, Kasahara K, Takahashi Y, Ohno Y (1999) Experimental evaluation of impact ionization coefficients in GaN. IEEE Electron Device Lett 20:608–610

Luschas M, Judaschke R, Luy JF (2002a) Measurement results of packaged millimeter-wave silicon IMPATT diodes. In: Proceedings of 27th international conference on infrared and millimeter waves, conference digest, pp 135–136

Luschas M, Judaschke R, Luy JF (2002b) Simulation and measurement results of 150 GHz integrated silicon IMPATT diodes. In: IEEE MTT-S international microwave symposium digest, pp 1269–1272

Luy JF, Casel A, Behr W, Kasper E (1987) A 90-GHz double-drift IMPATT diode made with Si MBE. IEEE Trans Electron Devices 34:1084–1089

Maestrini A, Mehdi I, Siles JV, Ward J, Lin R, Thomas B, Lee C, Gill J, Chattopadhyay G, Schlecht E, Pearson J, Siegel P (2012) First demonstration of a tunable electronic source in the 2.5–2.7 THz range. IEEE Trans Terahertz Sci Technol 3:177–185

Midford TA, Bernick RL (1979) Millimeter wave CW IMPATT diodes and oscillators. IEEE Trans Microw Theory Technol 27:483–492

Mukherjee M, Mazumder N (2007) Optically illuminated 4H-SiC terahertz IMPATT device. Egypt J Solids 30:87–101

Mukherjee M, Mazumder N, Roy SK, Goswami K (2007) Terahertz frequency performance of double drift impatt diode based on opto-sensitive semiconductor. In: Proceedings of asia-pacific microwave conference, pp 1–4

Mukherjee M, Mazumder N, Roy SK (2009) Prospects of 4H-SiC double drift region IMPATT device as a photo-sensitive high-power source at 0.7 terahertz frequency regime. Act Passive Electron Compon 2008:1–9

Mukherjee M, Banerjee S, Banerjee JP (2010) Dynamic characteristics of III–V and IV–IV semiconductor based transit time devices in the terahertz regime: a comparative analysis. Terahertz Sci Technol 3:98–109

Panda AK, Pavlidis D, Alekseev E (2001) DC and high-frequency characteristics of GaN-based IMPATTs. IEEE Trans Electron Devices 48:820–823

Panda AK, Parida RK, Agarwala NC, Dash GN (2007) A comparative study on the high band gap materials(GaN and SiC)- based IMPATTs. In: Proceedings of Asia-Pacific Microwave Conference, pp 1–4

Roy SK, Sridharan M, Ghosh R, Pal BB (1979) Computer method for the DC field and carrier current profiles in the IMPATT device starting from the field extremum in the depletion layer. In: Miller JH (ed) Proceedings of the 1st conference on numerical analysis of semiconductor devices (NASECODE I), Dublin, Ireland, pp 266–274

Roy SK, Banerjee JP, Pati SP (1985) A Computer analysis of the distribution of high frequency negative resistance in the depletion layer of IMPATT diodes. In: Proceedings 4th conference on numerical analyses of semiconductor devices (NASECODE IV), Dublin, Boole, pp 494–500

Scharfetter DL, Gummel HK (1969) Large-signal analysis of a silicon read diode oscillator. IEEE Trans Electron Devices 16:64–77

Shih HD, Bayraktaroglu B, Duncan WM (1983) Growth of millimeter-wave GaAs IMPATT structures by molecular beam epitaxy. J Vacuum Sci Technol B Microelectron Nanometer Struct 1:199–201

Shiyu SC, Wang G (2008) High-field properties of carrier transport in bulk wurtzite GaN: monte Carlo perspective. J Appl Phys 103:703–708

Siegel PH (2004) Terahertz technology in biology and medicine. IEEE Trans Microw Theory Tech 52:2438–2447

Siegel PH (2007) THz Instruments for Space. IEEE Trans Antenn Propag 55:2957–2965

Stoik CD, Bohn MJ, Blackshire JL (2008) Nondestructive evaluation of aircraft composites using transmissive terahertz time domain spectroscopy. Opt Express 16:17039–17051

Sze SM, Ng KK (2010) Physics of semiconductor devices. India, Willy

Sze SM, Ryder RM (1971) Microwave avalanche diodes. Proc IEEE Special Issue Microwave Semicond Devices 59:1140–1154

Tschernitz M, Freyer J (1995) 140 GHz GaAs double-Read IMPATT diodes. Electronic Lett 31:582–583

Umebu I, Chowdhury ANMM, Robson PN (1980) Ionization coefficients measured in abrupt InP junction. Appl Phys Lett 36:302–303

Vassilevski KV, Zekentes K, Zorenko AV, Romanov LP (2000) Experimental determination of electron drift velocity in 4H-SiC p^+–n–n^+ avalanche diodes. IEEE Electron Device Lett 21:485–487

Vassilevski KV, Zorenko AV, Zekentes K, Tsagaraki K, Bano E, Banc C, Lebedev A (2001) 4H-SiC IMPATT diode fabrication and testing. In: technical digest of international conference on SiC and related materials, Tsukuba, Japan, pp 713–714

Ward J, Schlecht E, Chattopadhyay G, Maestrini A, Gill J, Maiwald F, Javadi H, Mehdi I (2004) Capability of THz Sources based on Schotiky diode frequency multiplier chains. IEEE MTT-S Digest 3:1587–1590

Wollitzer M, Buchler J, Schafflr F, Luy JF (1996) D-band Si-IMPATT diodes with 300 mW CW output power at 140 GHz. Electronic Lett 32:122–123

Yasui T, Yasuda T, Sawanaka K, Araki T (2005) Terahertz paintmeter for noncontact monitoring of thickness and drying progress in paint film. Appl Opt 44:6849–6856

Yuan L, James A, Cooper JA, Melloch MR, Webb KJ (2001) Experimental demonstration of a silicon carbide IMPATT oscillator. IEEE Electron Device Lett 22:266–268